Structural topology optimization with strength and heat conduction constraints

Akihiro Takezawa[a,*], Gil Ho Yoon[b], Seung Hyun Jeong[c], Makoto Kobashi[d], Mitsuru Kitamura[a]

[a]*Division of Mechanical Systems and Applied Mechanics, Institute of Engineering, Hiroshima University, 1-4-1 Kagamiyama, Higashi-Hiroshima, Hiroshima, Japan*
[b]*School of Mechanical Engineering, Hanyang University, 222 Wangsimni-ro, Seongdong-gu, Seoul, Korea*
[c]*Graduate School of Mechanical Engineering, Hanyang University, 222 Wangsimni-ro, Seongdong-gu, Seoul, Korea*
[d]*Department of Materials Engineering, Graduate School of Engineering, Nagoya University, Furo-cho, Chikusa-ku, Nagoya, Japan*

Abstract

In this research, a topology optimization with constraints of structural strength and thermal conductivity is proposed. The coupled static linear elastic and heat conduction equations of state are considered. The optimization problem was formulated; viz., minimizing the volume under the constraints of p-norm stress and thermal compliance introducing the qp-relaxation method to avoid the singularity of stress-constraint topology optimization. The proposed optimization methodology is implemented employing the commonly used solid isotropic material with penalization (SIMP) method of topology optimization. The density function is updated using sequential linear programming

*Corresponding author. Tel: +81-82-424-7544; Fax: +81-82-422-7194
Email addresses: akihiro@hiroshima-u.ac.jp (Akihiro Takezawa), ghy@hanyang.ac.kr (Gil Ho Yoon), sh.jeong1985@gmail.com (Seung Hyun Jeong), kobashi@numse.nagoya-u.ac.jp (Makoto Kobashi), kitamura@hiroshima-u.ac.jp (Mitsuru Kitamura)

(SLP) in the early stage of optimization. In the latter stage of optimization, the phase field method is employed to update the density function and obtain clear optimal shapes without intermediate densities. Numerical examples are provided to illustrate the validity and utility of the proposed methodology. Through these numerical studies, the dependency of the optima to the target temperature range due to the thermal expansion is confirmed. The issue of stress concentration due to the thermal expansion problem in the use of the structure in a wide temperature range is also clarified, and resolved by introducing a multi-stress constraint corresponding to several thermal conditions.
Keywords: Topology optimization, Stress constraints, Heat conduction, Thermal expansion, Sensitivity analysis

1. Introduction

Static strength and heat conduction are two important issues in the design of mechanical structures. When strength is insufficient to support an applied load, a structure can suffer serious damage or break completely in the worst case. When heat conduction is insufficient for heat to dissipate from a certain heat source, the temperature may increase until there is injury to users or damage to surrounding devices. These criteria must sometimes be discussed together for one mechanical part. For example, automotive engine blocks are a typical structure requiring (1) strength supporting the load generated by an explosion and loads from mechanical movements of the internal and external parts and (2) heat conduction to release heat from an explosion to the air for the sake of efficient running. On the other hand, recent small electric devices containing central processing units, which can be a serious

heat source, have similar requirements. Because of the limited space of such a device, the shell must perform the structural role of supporting the electric part from external loads and the role of a heat sink to release heat generated by the central processing unit into the open air simultaneously. Moreover, the two performance criteria are closely related through the phenomenon of thermal expansion.

Recently, topology optimization (TO) [1, 2] has greatly assisted the development of novel mechanical structures because it enables fundamental shape optimization even for a complicated physical problem in topology. The strength of a structure is usually evaluated as a nominal stress that must not exceed a certain limit. To prevent these failures, a practical engineering approach is to calculate the nominal stress values of a structure of interest employing the finite element method (FEM) and to confine them to a certain maximum value by changing the geometry or the material of the structure.

Constructing a TO that minimizes volume subject to stress constraints has been regarded as a very difficult problem for many reasons, including the singularity issue and the local behavior of the stress constraints [3, 4, 5, 6, 7, 8, 9, 10, 11, 12, 13, 14, 15, 16]. First, according to previous research, discontinuities arise when a design variable of the solid isotropic material with penalization (SIMP) method converges to zero to simulate non-structural regions ("void" regions). When the design variables of some finite elements converge to zero, the stresses of the corresponding elements converge to finite values. If the stress of these elements reaches the specified stress limit, the elements will remain as a structural member to satisfy the

stress constraint. From a structural point of view, however, the stress values of the finite elements simulating the non-structural regions should be zero; i.e., no structure and no stress. Thus, the global optima can be obtained only by eliminating such elements. A local optimal topology with members violating the stress constraint is called a singular optimum. Such singularity of optima in TO was first observed by Sved and Ginos [17] using a simple three-bar truss example under multiple loading conditions. Cheng and Jiang [18] then determined that the fundamental reason for this observation were the discontinuities of the stress constraints at the zero cross-sectional area. There have been many solutions and relaxation methods proposed to avoid singular optima and obtain a global optimum numerically such as the epsilon relaxation method [4, 5], the qp-relaxation method [7, 8], and the relaxed stress indicator method [10]. Introducing TO methodology without intermediate density like the level-set method or evolutionary TO is also an effective way to avoid singular optima [6, 11].

Second, as the nominal stress values of all finite elements of interest must be constrained, from a computational point of view there are too many constraints to efficiently solve the optimization problem with a dual optimizer. As the computational cost for sensitivity analysis and sub-optimization increases, one must resort to approximation methods and other remedies. One such method is the constraint selection method, which selects only active stress constraints and calculates their sensitivity values. Recently, methods of representing a stress measure (sometimes called a global stress measure) have been proposed [9, 10, 14, 16]. In these approximation methods, rather than considering all the constraints, one or several global constraint func-

tions indirectly reflecting the behaviors and effects of the locally defined stress constraints are used. As only some constraint values and the corresponding sensitivity values are calculated, it becomes important to choose an appropriate form for the approximated global stress measure. Until now, the proposals have been the p-norm approach or the Kreisselmeier–Steinhauser (KS) approach [9, 10], a global stress measure based on boundary curvatures [14] and a global stress measure based on stress gradients [14, 16]. Moreover, the stress criterion represented as a functional over the whole domain is useful for sensitivity analysis using the adjoint method [19].

On the other hand, the heat conduction optimization problem has been handled from the early age of TO as a benchmark problem [2, 20, 21]. Steady-state heat conduction problems are the most basic problems [22, 23, 24, 25]. Starting with them, further research handling more practical engineering problems such as the multi-loading problem [26] or heat dissipation on a surface [27] were proposed. Incidentally, thermal optimization problems were actively researched also for the heat conduction problem (e.g., [28, 29]).

Structural and thermal problems are closely related through the phenomenon of thermal expansion. TO is greatly helpful for this kind of multiphysics problem because the design difficulty comes from the mechanical complexity. In previous studies, the structural stiffness or strength was optimized under various thermal conditions, such as stiffness maximization under fixed temperature [30, 31, 32], stress minimization under a design-dependent temperature field [33] and compliance minimization [34, 35]. As the latest example, stress-constrained optimization under fixed temperature was proposed by Deaton and Grandhi [36]. In the context of multi-objective optimization,

optimization for uniform stress and heat flux distributions [37] and maximization of both stiffness and heat conduction [38] have been studied. Note that the structural and thermal coupling problem was actively discussed also for the optimal design of a thermal actuator (e.g., [39, 40]). However, despite the large quantity of existing research, stress-constrained optimization under a design-dependent temperature field considering the thermal expansion effect remains an open problem.

In this research, according to the practical requirement of the mechanical structure mentioned first, TO under strength and thermal conductivity constraints was constructed. As the strength and heat conductivity criteria, p-norm and thermal compliance were introduced respectively in handling the stress-constrained optimization in a design-dependent temperature field. This work is organized as follows. The coupled static linear elastic and heat conduction equations of state are first considered. The proposed methodology is implemented employing the commonly used SIMP method of TO. The relationship between the physical properties of the material and the density function is defined and the sensitivity of the objective function with respect to the density function is calculated. The qp-relaxation method that avoids the singularity of the stress constraint is then introduced. The optimization problem is then formulated; viz., minimizing the volume under the p-norm von Mises stress and thermal compliance constraints. The density function is updated using sequential linear programming (SLP) in the early stage of the optimization. In the latter stage of the optimization, the phase field method (PFM) [15, 41] updates the density function to obtain clear optimal shapes without intermediate densities. We provide numerical examples to illustrate

the validity and utility of the proposed methodology.

2. Formulation

2.1. Equations of state

Initially we consider the equations of state pertaining to the linear elastic problem including the thermal expansion effect and heat conduction problem. Let us consider a linear elastic domain Ω with fixed displacement boundary Γ_{u0} and fixed temperature boundary Γ_{T0}, where there are surface force $\mathbf{t}$ and surface heat flux h at the boundaries Γ_f and Γ_h shown in Fig. 1. Other boundaries are traction free and thermal insulation. Ignoring time-dependent effects, only the equilibrium state is considered, and all materials are assumed to be isotropic. The basic equations of state for structural and thermal conduction are

$$-\nabla \cdot \boldsymbol{\sigma}(\mathbf{u}) = \mathbf{0}, \tag{1}$$

$$\mathbf{u} = \mathbf{0} \text{ on } \Gamma_{u0}, \tag{2}$$

$$-\nabla \cdot (k \nabla T) = 0, \tag{3}$$

$$T = T_0 \text{ on } \Gamma_{T0}, \tag{4}$$

where $\mathbf{u}$ is a displacement vector, $\boldsymbol{\sigma}$ is a stress tensor, T is temperature, T_0 is the prescribed temperature on Γ_{T0} and k is heat conductivity.

In the thermoelastic phenomenon, $\boldsymbol{\sigma}$ is coupled by the equations

$$\boldsymbol{\sigma} = \mathbf{C}\left(\boldsymbol{\varepsilon} - \boldsymbol{\varepsilon}_{\mathrm{th}}\right), \tag{5}$$

where

$$\boldsymbol{\varepsilon} = \frac{1}{2}\left\{\nabla\mathbf{u} + (\nabla\mathbf{u})^T\right\}, \tag{6}$$

$$\boldsymbol{\varepsilon}_{\mathrm{th}}(T) = \gamma(T - T_{\mathrm{ref}})\boldsymbol{\delta}, \tag{7}$$

where $\boldsymbol{\varepsilon}$ is a strain tensor, $\boldsymbol{\varepsilon}_{\mathrm{th}}$ is a thermal strain tensor, $\mathbf{C}$ is an elastic tensor, γ is a thermal expansion coefficient, T_{ref} is a reference temperature of thermal expansion, and $\boldsymbol{\delta}$ is Kronecker's delta. We reformulate Eqs. (1) and (3) to their weak form to solve them by FEM:

$$a(\mathbf{u}, \bar{\mathbf{u}}) = \alpha(T, \bar{\mathbf{u}}) + l_f(\bar{\mathbf{u}}), \text{ for } \mathbf{u} \in \mathbb{V}(\Omega), \ \forall\bar{\mathbf{u}} \in \mathbb{V}(\Omega) \tag{8}$$

$$b(T, \bar{T}) = l_h(\bar{T}), \text{ for } T \in H^1(\Omega), \ \forall\bar{T} \in H_0^1(\Omega) \tag{9}$$

where

$$\mathbb{V} = \{\mathbf{v} \in H^1(\Omega)^N \mid \mathbf{v} = 0 \text{ on } \Gamma_{u0}\} \tag{10}$$

$$a(\mathbf{u}, \bar{\mathbf{u}}) = \int_\Omega \boldsymbol{\varepsilon}(\mathbf{u})\mathbf{C}\boldsymbol{\varepsilon}(\bar{\mathbf{u}})\mathrm{d}x \tag{11}$$

$$\alpha(T, \bar{\mathbf{u}}) = \int_\Omega \boldsymbol{\varepsilon}_{\mathrm{th}}(T)\mathbf{C}\boldsymbol{\varepsilon}(\bar{\mathbf{u}})\mathrm{d}x, \tag{12}$$

$$l_f(\bar{\mathbf{u}}) = \int_{\Gamma_f} \mathbf{t}\bar{\mathbf{u}}\mathrm{d}s, \tag{13}$$

$$\boldsymbol{\varepsilon}_{\mathrm{th}}(T) = \gamma(T - T_{\mathrm{ref}})\boldsymbol{\delta}, \tag{14}$$

$$b(T, \bar{T}) = \int_\Omega k\nabla T \cdot \nabla\bar{T}\mathrm{d}x, \tag{15}$$

$$l_h(\bar{T}) = \int_{\Gamma_h} h\bar{T}\mathrm{d}s, \tag{16}$$

where Ω is the analysis domain, $\bar{\cdot}$ indicates a test function, $\mathbf{t}$ is a surface force vector on the boundary Γ_f, h is surface heat flux on the boundary Γ_h, $\mathbb{V}(\Omega)$

is a space of admissible displacements, $H^1(\Omega)$ is a Sobolev space, $H_0^1(\Omega)$ is the sub space of functions of $H^1(\Omega)$ that are zero on Γ_{T0}, N is the space dimension and T_{ref} is the reference temperature of thermal expansion.

By considering the Direcret boundary conditions in Eqs. (2) and (4), Eqs. (8) and (9) can be solved with respect to state variable $\mathbf{u}$ and T. Note that the coupling only exists in the structural equation in Eq. (8). Thus, there is weak coupling and a definite solution can be obtained by solving Eqs. (8) and (9) separately in sequence.

Figure 1 is about here.

2.2. Topology optimization

The TO method is used to optimize the geometry of the domain Ω, because this method can perform fundamental optimizations over arbitrary domains including shape and topology; *viz.*, the number of holes. The fundamental idea is to introduce a fixed, extended design domain D that includes *a priori* the optimal shape Ω_{opt} and the use of the characteristic function

$$\chi(\mathbf{x}) = \begin{cases} 1 & \text{if} \quad \mathbf{x} \in \Omega_{\text{opt}} \\ 0 & \text{if} \quad \mathbf{x} \in D \setminus \Omega_{\text{opt}} \end{cases} \tag{17}$$

Using this function, the original design problem of Ω is replaced by a material distribution problem incorporating a physical property, χA, in the extended design domain D, where A is an arbitrary physical property of the original material of Ω. Unfortunately, the optimization problem does not have any

optimal solutions [21]. A homogenization method is used to relax the solution space [1, 21]. In this way, the original material distribution optimization problem with respect to the characteristic function is replaced by an optimization problem of the "composite" consisting of the original material and a material with very low physical properties (e.g., Young's modulus or thermal conductivity), mimicking voids with respect to the density function. This density function represents the volume fraction of the original material and can be regarded as a weak limit of the characteristic function. In the optimization problem, the relationship between the material properties of the composite and the density function must be defined. The most popular approach, which sets a penalized proportional material property [42, 43], is the SIMP method. In this paper, employing the concept of the SIMP method, the relationships between the three material properties of the composite used in thermoelectric analysis (*i.e.*, Young's modulus E and thermal conductivity k) and the density function are set according to a simple equation with the penalized material density:

$$E^* = \rho^{p_E} E_{\mathrm{o}}, \tag{18}$$

$$k^* = \rho^{p_k} k_{\mathrm{o}}, \tag{19}$$

with

$$0 \leq \rho(\mathbf{x}) \leq 1, \ \mathbf{x} \in \Omega, \tag{20}$$

where the superscript suffix * signifies that the material property relates to the composite, the subscript suffix $_{\mathrm{o}}$ signifies that the material property relates to the original material, and p_E and p_k are positive penalization parameters.

Note that the thermal expansion coefficient γ is also a physical property that can be determined by the density function ρ. However, if we set γ as the function of ρ, thermal expansion in Eq. (7) is affected by the density function doubly from the heat conduction effect and thermal expansion and the optimization problem becomes more complex. To avoid this, we set γ as a fixed coefficient independent of ρ as done in [39, 40].

2.3. qp-relaxation method for the singularity issue

In this research, we introduce the von Mises stress σ_{VM} as the stress criterion formulated as

$$\sigma_{\mathrm{VM}} = \sqrt{\begin{aligned}&\frac{1}{2}\{(\sigma_{xx}-\sigma_{yy})^2+(\sigma_{yy}-\sigma_{zz})^2+(\sigma_{zz}-\sigma_{xx})^2\\&+3(2\sigma_{xy}^2+2\sigma_{yz}^2+2\sigma_{zx}^2)\}\end{aligned}}. \tag{21}$$

A fundamental issue of the stress-constrained volume minimization TO of continua is the so-called "singularity phenomenon" [4, 5, 44]. This comes from the discontinuous nature of the stress when the density function tends to zero, which corresponds to voids. Although the stress constraint becomes meaningless in the void in principle, numerical optimization algorithms cannot reach this point because the stress constraint might be violated as the density function is reduced. Thus, the stress constraint becomes discontinuous at zero density.

To resolve this issue, some methodologies relaxing the discontinuity, such as the epsilon relaxation method [4, 5] and the qp-relaxation method [7, 8], have been proposed. We introduced the qp-relaxation method in this research to resolve the singularity issue. In this methodology, the stress constraint is

formulated as

$$\sigma_{\mathrm{VM}} - \rho^q \sigma_{\mathrm{allow}} \leq 0, \tag{22}$$

where

$$q < p_E, \tag{23}$$

and q is a positive parameter and σ_{allow} is the allowable stress. According to this formula, the stress constraint can be kept feasible as the density function tends to zero. That is, the stress constraint vanishes in the void region.

2.4. Global stress criterion

When considering the structural optimization problem of ensuring the maximum stress is lower than the specified allowable stress with a minimum volume or weight, the straight-forward formulation is the minimization of the volume under the maximum-stress constraint. In this case, the maximum-stress location can jump to a different place during the optimization. That is, the constraint can be discontinuous through the optimization process and the convergence of the optimization problem could seriously be worse. To prevent this issue from arising, we introduced the so-called p-norm global stress criterion or KS approach [9, 10] which was used in our previous study [15]. In this approach, the stress criterion is formulated as

$$\langle \sigma_{\mathrm{PN}} \rangle = \left\{ \int_{\Omega} (\sigma_{\mathrm{VM}})^p \, \mathrm{d}x \right\}^{\frac{1}{p}}, \tag{24}$$

where p is the stress norm parameter. As the parameter $p \to \infty$, $\langle \sigma_{\mathrm{PN}} \rangle$ approaches $\max(\sigma_{\mathrm{VM}})$, and as the parameter $p \to 1$, $\langle \sigma_{\mathrm{PN}} \rangle$ approaches "Average value of σ_{VM} $\times$ Volume of Ω". If a large value was set for the parameter

p, an efficient optimization would be achieved since the approximated stress constraint approaches the original maximum stress constraint. However, the smoothness of the function is reduced by the large p, and more iterations are needed until convergence than in the case of small p. The relationship among the parameter p, solution quality and convergency is clearly presented in [10]. An appropriate value of p must set under the trade-off relationship between solution quality and convergency.

Finally, including the qp-relaxation form of the stress constraint in Eq. (22), the stress constraint introduced in this research is formulated:

$$\overline{\langle \sigma_{\mathrm{PN}} \rangle} - 1 = \left\{ \int_{\Omega} \left(\frac{\sigma_{\mathrm{VM}}}{\rho^q \sigma_{\mathrm{allow}}} \right)^p \mathrm{d}x \right\}^{\frac{1}{p}} - 1 \leq 0. \tag{25}$$

When the parameter p is not sufficiently large, there is a difference between the p-norm stress $\langle \sigma_{\mathrm{PN}} \rangle$ and the maximum stress. Thus, the optimal structure obtained under the constraint in Eq. (25) might not have maximum stress close to the allowable stress. In the case that the p-norm stress is lower than the maximum value, the resulting structure must have maximum stress exceeding the allowable stress and the structure is thus not sufficiently strong. In the case that the p-norm stress is higher than the maximum value, the resulting structure must have maximum stress less than the allowable stress and the structure thus has excess volume [10]. However, it is difficult to set a high value of p because it reduces the convergence performance. To overcome this problem and obtain a structure with a small stress difference between the p-norm and maximum stress while maintaining convergency, the allowable stress is relaxed by introducing the coefficient w calculated in each

iteration [10]:

$$w\overline{\langle\sigma_{\mathrm{PN}}\rangle} - 1 \leq 0, \tag{26}$$

where

$$w^{\mathrm{iter}} = \beta^{\mathrm{iter}} \frac{\max(\sigma_{\mathrm{VM}}^{\mathrm{iter}-1})}{\overline{\langle\sigma_{\mathrm{PN}}\rangle}^{\mathrm{iter}-1}} + (1-\beta^{\mathrm{iter}}) w^{\mathrm{iter}-1}, \tag{27}$$

and the superscript suffix $^{\mathrm{iter}}$ represents the value in the current optimization iteration and β is a parameter that controls the variation between w^{iter} and $w^{\mathrm{iter}-1}$.

2.5. Optimization problem

In addition to the above stress criterion, a thermal compliance [25] that is formulated as the boundary integration of the product of the surface heat flux and the temperature is introduced as a constraint for heat conduction:

$$c_h = \int_{\Gamma_h} hT \mathrm{d}s. \tag{28}$$

Because the heat flux h is the fixed value, the thermal compliance can be substantially used as the criterion of the average temperature of the boundary. We formulate the optimization problem as a volume minimization problem under the stress and heat conduction constraints:

$$\text{minimize}\, V(\rho) = \int_{\Omega} \rho \mathrm{d}x, \tag{29}$$

subject to

$$\text{Eqs. (25) and (26)}$$

$$\frac{c_h}{c_{\mathrm{allow}}} \leq 1 \tag{30}$$

$$0 < \rho \leq 1, \tag{31}$$

where c_{allow} is the allowable thermal compliance.

The advantages of including strength and thermal performance measures as constraints are the elimination of pathological structures with densities too low to meet the criteria of the design space [11] and the similarity with actual design problems.

2.6. Sensitivity analysis

To perform optimizations, we used the SLP technique, which requires first-order sensitivity analysis of the objective function and constraints with respect to the design variable ρ. Since the derivation is lengthy, only the results are shown here and the detailed derivation is presented in the Appendix.

The adjoint variables $\mathbf{r}$ and s are introduced to evaluate the sensitivity of the constraints, which depends on the two state variables $\mathbf{u}$ and T. The sensitivity of the stress p-norm in Eq. (25) with respect to ρ is

$$\overline{\langle \sigma_{\text{PN}} \rangle}'(\rho) = \frac{\langle \sigma_{\text{PN}} \rangle}{pg(\rho)} f'(\rho), \tag{32}$$

where

$$f(\rho) = \int_\Omega \left(\frac{\sigma_{\text{VM}}}{\rho^q \sigma_{\text{allow}}} \right)^p \mathrm{d}x, \tag{33}$$

$$f'(\rho) = \rho^{p-q-1} \left(\frac{\sigma_{\text{VM}}}{\sigma_{\text{allow}}} \right)^p + \varepsilon(\mathbf{u})^T \mathbf{C}'(\phi) \varepsilon(\mathbf{r}) - \boldsymbol{\varepsilon}_{\text{th}}(T) \mathbf{C}'(\phi) \boldsymbol{\varepsilon}(\mathbf{r}) - k'(\rho) \nabla T \cdot \nabla s, \tag{34}$$

and adjoint variables $\mathbf{r}$ and s satisfy the adjoint equations

$$\int_\Omega \frac{p}{\rho^q \sigma_{\text{VM}}} \left(\frac{\sigma_{\text{VM}}}{\sigma_{\max}} \right)^p \frac{\partial \sigma_{\text{VM}}}{\partial \boldsymbol{\sigma}} \mathbf{D} \boldsymbol{\varepsilon}(\bar{\mathbf{u}}) \mathrm{d}x - a(\bar{\mathbf{u}}, \mathbf{r}) = 0, \tag{35}$$

$$- \int_\Omega \frac{p}{\rho^q \sigma_{\text{VM}}} \left(\frac{\sigma_{\text{VM}}}{\sigma_{\max}} \right)^p \frac{\partial \sigma_{\text{VM}}}{\partial \boldsymbol{\sigma}} \mathbf{D} \boldsymbol{\varepsilon}_{\text{th}}(\bar{T}) \mathrm{d}x - \alpha(\bar{T}, \mathbf{r}) + A(q, \bar{T}) = 0, \tag{36}$$

where

$$\frac{\partial \sigma_{\mathrm{VM}}}{\partial \boldsymbol{\sigma}} = \left[\frac{2\sigma_x - \sigma_y - \sigma_z}{2\sigma_{\mathrm{VM}}} \ \frac{2\sigma_y - \sigma_x - \sigma_z}{2\sigma_{\mathrm{VM}}} \ \frac{2\sigma_z - \sigma_x - \sigma_y}{2\sigma_{\mathrm{VM}}} \ \frac{3\sigma_{xy}}{\sigma_{\mathrm{VM}}} \ \frac{3\sigma_{yz}}{\sigma_{\mathrm{VM}}} \ \frac{3\sigma_{zx}}{\sigma_{\mathrm{VM}}} \right]^T, \tag{37}$$

and $\mathbf{D}$ is the elastic coefficient tensor.

On the other hand, the sensitivity analysis of the thermal compliance c_h is a self-adjoint problem. Thus, the sensitivity is calculated without introducing an adjoint variable:

$$c_h'(\rho) = -k'(\rho)\nabla T \cdot \nabla T. \tag{38}$$

3. Numerical Implementation

3.1. Algorithm

The optimization is performed using an algorithm incorporating the sensitivity calculation and updating the design variable with SLP and the PFM [15, 41]. SLP is used in the early stage of optimization with the so-called density filter [45]. The PFM is used in the latter stage of optimization to obtain clear optimal shapes without intermediate densities. The optimization algorithm is presented in Fig. 2.

Figure 2 is about here.

3.2. Phase field method for shape optimization

The PFM for shape optimization [15, 41], which is used in the latter stage of the optimization procedure, is outlined. The method uses the identical domain representation and sensitivity analysis as the density function with the

SIMP-based TO. In contrast to the ordinary SIMP method, in which the design variable is updated employing gradient-based optimization, the density function is updated by solving the so-called Allen-Cahn partial differential equation in the PFM:

$$\frac{\partial \rho}{\partial t} = \kappa \nabla^2 \rho - P'(\rho), \tag{39}$$

with

$$P(\rho) = \frac{1}{4} Q(\rho) + \eta R(\rho), \tag{40}$$

$$Q(\rho) = \rho^2 (1 - \rho^2), \tag{41}$$

$$R(\rho) = \rho^3 (6\rho^2 - 15\rho + 10), \tag{42}$$

where t is the artificial time corresponding to the step size of the design variable, P is the asymmetric double-well potential sketched in Figure 3, and η is a positive variable. Note that P has two minima, at 0 and 1. Because of coupling between the diffusion and reaction terms in Equation (39), the density function ρ is divided into several domains corresponding to the value 0 or 1. The so-called phase field interface corresponding to the intermediate values $0 < \rho < 1$ exists between these domains. The interface moves in the normal direction according to the shape of the double-well potential. That is, the interface evolves in the direction of the lower minimum of the potential.

Owing to the mutual effects of the double-well potential and the diffusion term, the intermediate density of the optimal configuration is forced to converge to 0 or 1 outside the resulting new phase field interface. This effect is similar for the non-linear diffusion filtering method [46, 47]. The optimal configuration is then updated using the interface motion like in the latter stage of optimization.

Some papers use the sensitivity to choose the double-well potential gap that decides the moving direction of the phase field interface [15, 41, 48]. In this way, the constraint is embedded in the objective function using the Lagrange multiplier method. However, to handle the constraint effectively, the gap can be set according to the result of the SLP update [49]. Let us consider the minimization of the objective function $J(\mathbf{X})$ with an inequality constraint $g(\mathbf{X}) \leq 0$ with respect to a design variable vector $\mathbf{X} = [X_1, X_2, ..., X_n]$. In SLP, the increment $\Delta\mathbf{X}$ of the design variable $\mathbf{X}$ is obtained as the solution of a linear programming problem:

$$\text{minimize } J(\mathbf{X}) + \nabla J(\mathbf{X})^T \Delta\mathbf{X}, \tag{43}$$

subject to

$$g(\mathbf{X}) + \nabla g(\mathbf{X})^T \Delta\mathbf{X} \leq 0, \tag{44}$$

$$\Delta X_{\text{low}} \leq \Delta X_i \leq \Delta X_{\text{up}} \text{ for } i = 1, ..., n, \tag{45}$$

where ΔX_{low} and ΔX_{up} are respectively the lower and upper bounds of ΔX_i and the superscript suffix ^{T} denotes the transpose.

Figure 3 is about here.

4. Numerical Examples

The following numerical examples are provided to confirm the validity and utility of the proposed methodology. In all examples, the material is assumed

as a structural steel with Young's modulus of 210 GPa, Poison's ratio of 0.3, allowable stress of 358 MPa, thermal conductivity of 84 $\mathrm{Wm^{-1}K^{-1}}$ and a thermal expansion coefficient of $12.1\times10^{-6}\mathrm{K^{-1}}$. The domain is approximated as a two-dimensional plane stress model and the thickness of the domain is set to 1 mm. The reference temperature T_{ref} in Eq. (14) and the fixed temperature are set to 293 K. The optimization problem in Eqs. (29)–(31) is solved according to the algorithm set out in Fig. 2. The penalization parameters p_E and p_k in Equations (18) and (19) are both set to 3. The parameter q used in qp-relaxation in Eq. (22) is set to 2. The parameter p used in the p-norm calculation in Eq. (25) is set to 16. The positive coefficient η in Eq. (40) is set to 10. At each iteration, we perform a finite element analysis of the state equation and one update of the evolution equation for the phase field function by solving the finite difference equation of the semi-implicit scheme. The time step Δt is set to 0.9 times the limit of the Courant number. All finite element analyses are performed using the commercial software COMSOL Multiphysics for quick implementation of the proposed methodology, and to effectively solve the equations of state and adjoint with a multi-core processor. First-order iso-parametric Lagrange finite elements are used throughout. The von Mises stresses are calculated at the centers of all finite elements. The initial value of the density function is set to 1 uniformly.

4.1. Optimization of an L-shaped beam

For the first numerical example, an L-shaped beam that has sometimes been used as a benchmark problem is considered; see Fig. 4. The domain is discretized by a 1 mm×1 mm square mesh. Because of the stress concentra-

tion at the reentrant corner, there should be smooth boundaries there. Note that to prevent stress concentration in the loading region, the vertical 8000 Nm^{-2} load is distributed in the top region of the right arm. Surface heat flux of 85 Wm^{-2} is applied to the loading point. The limit of the thermal compliance is set to 3, corresponding to an average temperature of 300 K at the loading boundary. The density function is first updated 200 times by conventional SLP and then 200 times employing the SLP based PFM. The move limits of SLP are set to 0.02 and 0.01 as absolute increment values in the former and latter stages respectively.

Figure 4 is about here.

Figure 5 shows the optimal configuration and its von Mises stress and temperature distributions. Figure 6 shows the convergence history of the objective function and the constraints. After the 200th iteration, the constraints worked strictly and the volume increased as a result. Finally, the optimal solution had clear topology satisfying both constraints. The maximum value of von Mises stress was 360 MPa, which almost meets the requirement of allowable stress of 358 MPa.

Figures 5 and 6 are about here.

The mechanical aspect of the obtained optimal structure is compared with that of the optimal configurations under a single constraint. Figure 7 shows the optimal configuration of only considering the stress constraint

and its stress distribution and that only considering the thermal constraint and its temperature distribution. The surface heat flux and force are set to zero in structural and thermal optimization respectively. Other optimization conditions are set the same.

Figure 7 is about here.

The optimal configuration only considering the stress constraint has a nearly uniform stress distribution with a value close to the allowable stress. On the other hand, that only considering the thermal constraint has a simple shape to connect the heat source region and the fixed-temperature region. The optimal configuration for the multi-constraint problem shown in Fig. 5 can be considered to have both characteristics. As a result, the stress distribution was not uniform and the thermal root was not the shortest. However, the structure certainly satisfies both constraints.

Comparing with Figs. 5 and 7, the optimal configuration under multiple constraints definitely has more volume than those with a single constraint. To satisfy the stricter constraint, more structural volume seems to be required. To confirm this, the multi-constraint optimization is performed varying the surface force and heat flux. Figure 8 shows optimal configurations and volume for a fixed surface force of 8000 Nm^{-2} and varied surface heat flux of 0, 55, 65, 75 and 85 Wm^{-2}. Figure 9 shows the optimal configurations and volume under the fixed surface heat flux of 85 Wm^{-2} and varied surface forces of 0, 2000, 4000, 6000 and 8000 Nm^{-2}. Other optimization conditions were set the same. In both figures, more volume was required to satisfy the stricter

constraints. All the above optimization results are summarized in Table 1 for reference.

Figures 8 and 9 are about here.

Table 1: Summary of optimization results

Fig. No.	Surface force (Nm^{-2})	Heat flux (Wm^{-2})	Volume (m^3)	Const. in Eq. (26)	Maximum VM stress (MPa)	Const. in Eq. (30)	Average temperature of Γ_h (K)
Fig. 5	8000	85	3.90×10^{-3}	-1.16×10^{-2}	360.19	3.41×10^{-4}	300.10
Fig. 7 (a)	8000	0	2.30×10^{-3}	2.61×10^{-2}	360.51	-	-
Fig. 7 (b)	0	85	2.61×10^{-3}	-	-	7.2×10^{-4}	300.22
Fig. 8 (a)	8000	55	2.96×10^{-5}	-2.96×10^{-3}	357.10	1.52×10^{-4}	300.05
Fig. 8 (b)	8000	65	3.13×10^{-4}	4.39×10^{-3}	356.75	2.13×10^{-4}	300.06
Fig. 8 (c)	8000	75	3.51×10^{-3}	-2.49×10^{-3}	357.51	2.35×10^{-4}	300.07
Fig. 9 (a)	2000	85	2.67×10^{-3}	-6.53×10^{-3}	355.67	2.33×10^{-6}	300.00
Fig. 9 (b)	4000	85	3.45×10^{-3}	-7.95×10^{-3}	355.77	4.57×10^{-4}	300.14
Fig. 9 (c)	6000	85	3.63×10^{-3}	-2.49×10^{-3}	358.69	2.78×10^{-4}	300.08

4.2. Optimization of a bridge-like structure

In the first example, since the structure was fixed at only one boundary, the effect of thermal expansion seemed to be small. As the second example, we consider a bridge-like structure having fixed boundaries on both sides, as shown in Fig. 10, to study the effect of thermal expansion on the optimal configuration. The domain is discretized by a 1 mm $\times$ 1 mm square mesh. The loading region is set at the center of the bottom side and a vertical 40,000 Nm^{-2} load is distributed in this region. Surface heat flux of 100 Wm^{-2} is applied to the region on the right side. The limit of the thermal compliance is set to 6.1, corresponding to an average temperature of 305 K at the heat flux

boundary. The density function is first updated 200 times by conventional SLP and then 300 times employing the SLP-based PFM. The move limits of SLP are set to 0.02 and 0.01 as absolute increment values in the former and latter stages respectively, as in the previous example.

Figure 10 is about here.

Figure 11 shows the optimal configuration considering both structural and thermal problems and its von Mises stress and temperature distributions. Figure 12 shows the reference optimal configurations and related results only considering structural and thermal problems separately. The optimal configuration shown in 11 can be regarded as intermediate of the optimal configurations shown in Fig. 12 (a) and (c), as for the L-shaped problem.

Figures 11 and 12 are about here.

In this example, the optimization was performed in a low-temperature range around 300 K. Since 293 K is set as the reference temperature of thermal expansion in Eq. (7), the effect of thermal expansion might be slight. Thus, the optimization is next performed in a higher temperature range in which the thermal expansion effect might be more serious. Surface heat flux of 1000 Wm^{-2} is applied to the region on the right side. The limit of the thermal compliance is set to 8.26, corresponding to an average temperature of 413 K at the heat flux boundary. The temperature limit is set according to

the optimization setting of the low-temperature-range problem considering the linearity between the applied heat flux and the resulting temperature. When only considering the thermal problem, the same optimization results would be obtained in both temperature ranges under these settings. All other settings are the same as in the low-temperature-range example.

Figure 13 shows the optimal configuration obtained under the above conditions and its von Mises stress and temperature distributions.

Figure 13 is about here.

Clearly different topology from Fig. 12 was obtained owing to the reduction in the stress concentration due to thermal expansion. For reference, the optimization is also performed in a high-temperature range using the first L-shaped example. Surface heat flux of 1450 Wm^{-2} is applied to the loading point. The limit of the thermal compliance is set to 4.12, corresponding to an average temperature of 412 K at the loading boundary. Figure 14 shows the optimal configuration and its von Mises stress and temperature distributions.

Figure 14 is about here.

Even in the L-shaped example in which only one boundary is fixed, a shape different from that in the low-temperature range was obtained. However, since Figs. 14 and 5 have the same topology at least, the thermal expansion effect could be more serious in the bridge-like example. The optimization results for all the above bridge examples are summarized in Table 2 for reference.

Table 2: Summary of optimization results

Fig. No.	Surface force (Nm^{-2})	Heat flux (Wm^{-2})	Volume (m^3)	Const. in Eq. (26)	Maximum VM stress (MPa)	Const. in Eq. (30)	Average temperature of Γ_h (K)
Fig. 11	40000	100	7.00×10^{-3}	-2.75×10^{-3}	357.09	2.97×10^{-5}	305.01
Fig. 12 (a)	40000	0	3.66×10^{-3}	-9.64×10^{-4}	357.35	-	-
Fig. 12 (c)	0	100	5.55×10^{-3}	-	-	6.29×10^{-4}	305.19
Fig. 13	40000	1000	7.96×10^{-3}	1.19×10^{-3}	358.43	4.13×10^{-4}	413.17
Fig. 14	8000	1450	4.41×10^{-3}	-3.37×10^{-3}	358.37	-1.05×10^{-3}	411.57

4.3. Optimization under multi-thermal conditions

In a structure with both side fixed, as in the previous example, a design for high temperatures might not always work well at low temperatures because the structure suffers an expansion-like force at low temperatures even above the reference temperature range and this can be another source of stress concentration. To confirm this, 10 heat fluxes are applied in the range between the two heat fluxes used in the above optimizations. Figure 15 plots the maximum von Mises stress corresponding to each heat flux in optimal configurations of the L-shape and bridge-like examples obtained for low and high temperature ranges. In the L-shaped example, the maximum von Mises stress slightly increases in response to a heat flux increment for both low- and high-temperature optima. However, in the bridge example, in addition to the rapid increase in the maximum stress for the low-temperature optimum, the high-temperature optimum has a worse stress value with the lowest heat flux. The optimum obtained in the high-temperature range includes high thermal expansion in its design. Thus, without thermal expansion in a low-temperature environment, the structure suffers an expansion-like force even at temperatures above 293 K, which is the reference temperature of the thermal expansion. As a result, in such a structure, the optimal solu-

tion obtained for one temperature range only worked well for the specified temperature range. The structure designed to withstand high thermal expansion in a high-temperature environment would be damaged if the heat was removed. The methodology might thus be impractical for actual optimal design.

Figure 15 is about here.

To generate optima that work well in both high- and low-temperature environments for the bridge-like structure with both sides fixed, multi-stress constraints are introduced considering both low and high heat flux conditions. The equations of state are solved twice for low and high heat flux and two stress criteria are obtained. The optimization is performed until both constraints are satisfied. Using the design example shown in Fig. 10, two heat fluxes, 85 and 1450 Wm^{-2}, are applied separately. The temperature limit is set to 8.26 only considering a high heat flux condition. Other conditions are the same as in the previous example.

Figure 16 shows the optimal configuration and its von Mises stress distributions for the two heat flux conditions. The topology is the same as for the optimal configuration in the high-temperature range shown in Fig. 13, and the stress limit was certainly satisfied under both conditions. This optimization result is summarized in Table 3.

Figure 16 is about here.

Table 3: Summary of optimization results

Surface force (Nm^{-2})	Heat flux (Wm^{-2})	Volume (m^3)	Const. in Eq. (26)	Maximum VM stress (MPa)	Const. in Eq. (30)	Average temperature of Γ_h (K)
40000	1000	8.18×10^{-3}	2.31×10^{-2}	358.34	-2.19×10^{-3}	412.10
-	100	-	2.75×10^{-3}	358.62	-	304.91

The maximum stress is checked using 10 intervals of heat flux as in Fig. 15 although it is trivial considering the linearity of the thermal expansion. Figure 17 plots the maximum von Mises stress corresponding to each heat flux. The methodology introducing multiple stress constraints for high and low temperatures simultaneously can be said to work well for thermal stress relaxation in the range between two low and high temperatures.

Figure 17 is about here.

5. Conclusion

In this study, we developed a topology optimization (TO) under strength and heat conductivity constraints. The coupled static structural and thermal equations of state were considered and the optimization problem was then formulated; viz., minimizing the volume under the stress and thermal compliance constraints. The proposed optimization methodology was implemented employing the commonly used SIMP method of TO. The density function was updated using SLP in the early stage of the optimization. In the latter stage of the optimization, the PFM updates the density function to obtain clear optimal shapes without intermediate densities.

The optimization was successful for arbitrary two-dimensional shapes and structural and thermal conditions. In general, more volume was required for stricter constraints. In terms of the stress constraint, different shapes were obtained according to the resulting temperature of the optimal result owing to the effect of thermal expansion. In particular, this effect became more serious for the structure with both sides fixed. This kind of structure also had the drawback that it did not work well outside of the optimized temperature range in the case of either high- or low-temperature optimization. We also confirmed that this issue could be resolved by introducing multi-thermal conditions and stress constraints corresponding to both low- and-high temperature environments. A novel structure having good heat conductivity preventing damage from thermal expansion or compression in a wide temperature range could be obtained.

Appendix A. Sensitivity analysis

In this appendix, a detailed derivation of the sensitivities in Eqs. (34) and (38) the adjoint equations in Eqs. (35) and (36) is outlined according to the procedure described in Chapter 5 of [50]. We define the general objective or constraint function of a linear static thermoelastic problem as $J(\rho) = \int_\Omega j(\rho, \mathbf{u}, T)\mathrm{d}x$. The derivative of this function in the direction θ is then

$$\begin{aligned}\langle J'(\phi), \theta\rangle &= \int_\Omega j'(\phi)\theta\mathrm{d}x + \int_\Omega j'(\mathbf{u})\langle \mathbf{u}'(\phi), \theta\rangle\mathrm{d}x + \int_\Omega j'(T)\langle T'(\phi), \theta\rangle\mathrm{d}x \\ &= \int_\Omega j'(\phi)\theta\mathrm{d}x + \int_\Omega j'(\mathbf{u})\bar{\mathbf{v}}\mathrm{d}x + \int_\Omega j'(T)\bar{T}\mathrm{d}x,\end{aligned} \tag{A.1}$$

where $\bar{\mathbf{u}} = \langle \mathbf{u}'(\phi), \theta \rangle$, $\bar{T} = \langle T'(\phi), \theta \rangle$. Setting adjoint states $\mathbf{r}$ and s as test functions of the weak-form equations of state in Eqs. (8)-(16), the Lagrangian is formulated as

$$L(\phi, \mathbf{u}, T, \mathbf{r}, s) = \int_\Omega j(\mathbf{u}, T)\mathrm{d}x + a(\mathbf{u}, \mathbf{r}) - \alpha(T, \mathbf{r}) - l(\mathbf{r}) + A(T, s) - L(s). \quad \text{(A.2)}$$

Using this expression, the derivative of the objective function can be expressed as

$$\begin{aligned}
\langle j'(\phi), \theta \rangle =& \left\langle \frac{\partial L}{\partial \phi}(\phi, \mathbf{u}, T, \mathbf{r}, s), \theta \right\rangle + \left\langle \frac{\partial L}{\partial \mathbf{u}}(\phi, \mathbf{u}, T, \mathbf{r}, s), \langle \mathbf{u}'(\phi), \theta \rangle \right\rangle \\
&+ \left\langle \frac{\partial L}{\partial T}(\phi, \mathbf{u}, T, \mathbf{r}, s), \langle T'(\phi), \theta \rangle \right\rangle \\
=& \left\langle \frac{\partial L}{\partial \phi}(\phi, \mathbf{u}, T, \mathbf{r}, s), \theta \right\rangle + \left\langle \frac{\partial L}{\partial \mathbf{u}}(\phi, \mathbf{u}, T, \mathbf{r}, s), \bar{\mathbf{u}} \right\rangle + \left\langle \frac{\partial L}{\partial T}(\phi, \mathbf{u}, T, \mathbf{r}, s), \bar{T} \right\rangle \\
&.
\end{aligned} \quad \text{(A.3)}$$

Consider the case where the second and third terms are zero. These terms are calculated as

$$\left\langle \frac{\partial L}{\partial \mathbf{u}}, \bar{\mathbf{u}} \right\rangle = \int_\Omega j'(\mathbf{u})\bar{\mathbf{u}}\mathrm{d}x - a(\bar{\mathbf{u}}, \mathbf{r}) = 0, \quad \text{(A.4)}$$

$$\left\langle \frac{\partial L}{\partial T}, \bar{T} \right\rangle = \int_\Omega j'(T)\bar{T}\mathrm{d}x - \alpha(\bar{T}, \mathbf{r}) + A(s, \bar{T}) = 0. \quad \text{(A.5)}$$

When the adjoint states $\mathbf{r}$ and s satisfy the above adjoint equations, the second and third terms of Eq. (A.3) can be ignored. On the other hand, the derivatives of Eq. (8) with respect to ρ in the direction θ are

$$da(\mathbf{u}, \mathbf{r}) + a(\bar{\mathbf{u}}, \mathbf{r}) - \alpha(\bar{T}, \mathbf{r}) - d\alpha(T, \mathbf{r}) = 0, \quad \text{(A.6)}$$

where

$$da(\mathbf{u}, \mathbf{r}) = \int_{\Omega} \boldsymbol{\varepsilon}(\mathbf{u}) \mathbf{C}'(\phi) \boldsymbol{\varepsilon}(\mathbf{r}) \mathrm{d}x \tag{A.7}$$

$$d\alpha(T, \mathbf{r}) = \boldsymbol{\varepsilon}_{\mathrm{th}}(T) \mathbf{C}'(\phi) \boldsymbol{\varepsilon}(\mathbf{r}) \theta \mathrm{d}x. \tag{A.8}$$

The derivatives of Eq. (9) are

$$dA(T, s) + A(\bar{T}, s) = 0, \tag{A.9}$$

where

$$dA(T, s) = \int_{\Omega} \kappa'(\phi) \nabla T \cdot \nabla s \mathrm{d}x. \tag{A.10}$$

Substituting Eqs. (A.9) and (A.10) into Eqs. (A.4) and (A.5) and combining the equations, it follows that

$$\begin{aligned} &\int_{\Omega} j'(\mathbf{u}) \bar{\mathbf{u}} \mathrm{d}x + \int_{\Omega} j'(T) \bar{T} \mathrm{d}x \\ =&da(\mathbf{u}, \mathbf{r}) - d\alpha(T, \mathbf{r}) + dA(T, a). \end{aligned} \tag{A.11}$$

Substituting Eq. (A.11) into Eq. (A.1) yields

$$J'(\phi) = j'(\phi) + \varepsilon(\mathbf{u})^T \mathbf{C}'(\phi) \varepsilon(\mathbf{r}) - \boldsymbol{\varepsilon}_{\mathrm{th}}(T) \mathbf{C}'(\phi) \boldsymbol{\varepsilon}(\mathbf{r}) + \kappa'(\phi) \nabla T \cdot \nabla s. \tag{A.12}$$

Substituting the function $f(\rho)$ in Eq. (33), which is a part of the p-norm, into Eqs. (A.4), (A.5) and (A.12), the sensitivity in Eq. (34) and adjoint equations in Eqs. (35) and (36) are obtained. On the other hand, substituting the thermal compliance in Eq. (28) into Eqs. (A.4) and (A.5), it follows that

$$a(\bar{\mathbf{u}}, \mathbf{r}) = 0, \tag{A.13}$$

$$L(\bar{T}) - \alpha(\mathbf{r}, \bar{T}) + A(s, \bar{T}) = 0. \tag{A.14}$$

Since the result of Eq. (A.13) is $\mathbf{r} = \mathbf{0}$, the second term of Eq. (A.14) can be ignored. Equation (A.14) then equals Eq. (A.9) when its result is $s = -T$. Thus, this is the self-adjoint problem. Substituting Eq. (28), $\mathbf{r} = \mathbf{0}$ and $s = -T$ into Eq. (A.12), the sensitivity in Eq. (38) is obtained.

References

[1] M. P. Bendsøe, N. Kikuchi, Generating optimal topologies in structural design using a homogenization method, Comput. Meth. Appl. Mech. Eng. 71 (2) (1988) 197–224.

[2] M. P. Bendsøe, O. Sigmund, Topology Optimization: Theory, Methods, and Applications, Springer-Verlag, Berlin, 2003.

[3] R. J. Yang, C. J. Chen, Stress-based topology optimization, Struct. Optim. 12 (2-3) (1996) 98–105.

[4] G. D. Cheng, X. Guo, Epsilon-relaxed approach in structural topology optimization, Struct. Optim. 13 (1997) 258–266.

[5] P. Duysinx, M. P. Bendsøe, Topology optimization of continuum structures with local stress constraints, Int. J. Numer. Meth. Eng. 43 (8) (1998) 1453–1478.

[6] Q. Q. Liang, Y. M. Xie, G. P. Steven, Optimal selection of topologies for the minimum-weight design of continuum structures with stress constraints, Proc. IME C J. Mech. Eng. Sci. 213 (8) (1999) 755–762.

[7] M. Bruggi, On an alternative approach to stress constraints relaxation in topology optimization, Struct. Multidisc. Optim. 36 (2) (2008) 125–141.

[8] M. Bruggi, P. Venini, A mixed fem approach to stress-constrained topology optimization, Int. J. Numer. Meth. Eng. 73 (12) (2008) 1693–1714.

[9] J. Paris, F. Navarrina, I. Colominas, M. Casteleiro, Topology optimization of continuum structures with local and global stress constraints, Struct. Multidisc. Optim. 39 (4) (2009) 419–437.

[10] C. Le, J. Norato, T. Bruns, C. Ha, D. Tortorelli, Stress-based topology optimization for continua, Struct. Multidisc. Optim. 41 (4) (2010) 605–620.

[11] X. Guo, W. S. Zhang, M. Y. Wang, P. Wei, Stress-related topology optimization via level set approach, Comput. Meth. Appl. Mech. Eng. 200 (47) (2011) 3439–3452.

[12] S. H. Jeong, S. H. Park, D. H. Choi, G. H. Yoon, Topology optimization considering static failure theories for ductile and brittle materials, Comput. Struct. 110-111 (2012) 116–132.

[13] Y. Luo, Z. Kang, Topology optimization of continuum structures with drucker–prager yield stress constraints, Comput. Struct. 90 (2012) 65–75.

[14] W. S. Zhang, X. Guo, M. Y. Wang, P. Wei, Optimal topology design of continuum structures with stress concentration alleviation via level set method, Int. J. Numer. Meth. Eng. 93 (9) (2013) 942–959.

[15] S. H. Jeong, G. H. Yoon, A. Takezawa, D. H. Choi, Development of a novel phase-field method for local stress-based shape and topology optimization, Comput. Struct. 132 (2014) 84–98.

[16] X. Guo, W. Zhang, W. Zhong, Stress-related topology optimization of continuum structures involving multi-phase materials, Comput. Meth. Appl. Mech. Eng. 268 (2014) 632–655.

[17] G. Sved, Z. Ginos, Structural optimization under multiple loading, Int. J. Mech. Sci. 10 (10) (1968) 803–805.

[18] G. Cheng, Z. Jiang, Study on topology optimization with stress constraints, Eng. Optim. 20 (2) (1992) 129–148.

[19] E. J. Haug, K. K. Choi, V. Komkov, Design Sensitivity Analysis of Structural Systems, Academic Press, Orlando, 1986.

[20] A. Cherkaev, Variational Methods for Structural Optimization, Springer-Verlag, New York, 2000.

[21] G. Allaire, Shape Optimization by the Homogenization Method, Springer-Verlag, New York, 2001.

[22] Q. Li, G. P. Steven, O. M. Querin, Y. M. Xie, Shape and topology design for heat conduction by evolutionary structural optimization, Int. J. Heat Mass Tran. 42 (17) (1999) 3361–3371.

[23] J. Haslinger, A. Hillebrand, T. Kärkkäinen, M. Miettinen, Optimization of conducting structures by using the homogenization method, Struct. Multidisc. Optim. 24 (2) (2002) 125–140.

[24] Q. Li, G. P. Steven, Y. M. Xie, O. M. Querin, Evolutionary topology optimization for temperature reduction of heat conducting fields, Int. J. Heat Mass Tran. 47 (23) (2004) 5071–5083.

[25] A. Gersborg-Hansen, M. Bendsøe, O. Sigmund, Topology optimization of heat conduction problems using the finite volume method, Struct. Multidisc. Optim. 31 (4) (2006) 251–259.

[26] C. G. Zhuang, Z. H. Xiong, H. Ding, A level set method for topology optimization of heat conduction problem under multiple load cases, Comput. Meth. Appl. Mech. Eng. 196 (4) (2007) 1074–1084.

[27] T. Gao, W. H. Zhang, J. H. Zhu, Y. J. Xu, D. H. Bassir, Topology optimization of heat conduction problem involving design-dependent heat load effect, Finite Elem. Anal. Des. 44 (14) (2008) 805–813.

[28] A. Iga, S. Nishiwaki, K. Izui, M. Yoshimura, Topology optimization for thermal conductors considering design-dependent effects, including heat conduction and convection, Int. J. Heat Mass Tran. 52 (11) (2009) 2721–2732.

[29] G. H. Yoon, Topological design of heat dissipating structure with forced convective heat transfer, J. Mech. Sci. Tech. 24 (6) (2010) 1225–1233.

[30] H. Rodrigues, P. Fernandes, A material based model for topology optimization of thermoelastic structures, Int. J. Numer. Meth. Eng. 38 (12) (1995) 1951–1965.

[31] Q. Li, G. P. Steven, Y. M. Xie, Displacement minimization of thermoelastic structures by evolutionary thickness design, Comput. Meth. Appl. Mech. Eng. 179 (3) (1999) 361–378.

[32] J. D. Deaton, R. V. Grandhi, Stiffening of restrained thermal structures

via topology optimization, Struct Multidisc. Optim. 48 (4) (2013) 731–745.

[33] Q. Li, G. P. Steven, Y. M. Xie, Thermoelastic topology optimization for problems with varying temperature fields, J. Therm. Stresses 24 (4) (2001) 347–366.

[34] S. Cho, J. Y. Choi, Efficient topology optimization of thermo-elasticity problems using coupled field adjoint sensitivity analysis method, Finite Elem. Anal. Des. 41 (15) (2005) 1481–1495.

[35] T. Gao, W. Zhang, Topology optimization involving thermo-elastic stress loads, Struct Multidisc. Optim. 42 (5) (2010) 725–738.

[36] J. D. Deaton, R. V. Grandhi, Stress-based topology optimization of thermal structures, in: Proceedings of of the 10th World Congress on Structural and Multidisciplinary Optimization, 2013.

[37] Q. Li, G. P. Steven, O. M. Querin, Y. M. Xie, Structural topology design with multiple thermal criteria, Engng. Comput. 17 (6) (2000) 715–734.

[38] N. Kruijf, S. Zhou, Q. Li, Y. W. Mai, Topological design of structures and composite materials with multiobjectives, Int. J. Solid Struct. 44 (22) (2007) 7092–7109.

[39] J. Jonsmann, O. Sigmund, S. Bouwstra, Compliant thermal microactuators, Sensor. Actuator. Phys. 76 (1) (1999) 463–469.

[40] O. Sigmund, Design of multiphysics actuators using topology

optimization–part i: one-material structures, Comput. Meth. Appl. Mech. Eng. 190 (49-50) (2001) 6577–6604.

[41] A. Takezawa, S. Nishiwaki, M. Kitamura, Shape and topology optimization based on the phasefield method and sensitivity analysis, J. Comput. Phys. 229 (7) (2010) 2697–2718.

[42] M. P. Bendsøe, Optimal shape design as a material distribution problem, Struct. Optim. 1 (4) (1989) 193–202.

[43] M. Zhou, G. I. N. Rozvany, The coc algorithm. ii: Topological, geometrical and generalized shape optimization, Comput. Meth. Appl. Mech. Eng. 89 (1-3) (1991) 309–336.

[44] M. Ohsaki, Optimization of finite dimensional structures, CRC Press, Boca Raton, 2010.

[45] T. E. Bruns, O. Sigmund, D. A. Tortorelli, Numerical methods for the topology optimization of structures that exhibit snap-through, Int. J. Numer. Meth. Eng. 55 (10) (2002) 1215–1237.

[46] M. Y. Wang, S. Zhou, H. Ding, Nonlinear diffusions in topology optimization, Struct. Multidisc. Optim. 28 (4) (2004) 262–276.

[47] S. Zhou, Q. Li, Computational design of multi-phase microstructural materials for extremal conductivity, Comput. Mater. Sci. 43 (3) (2008) 549–564.

[48] A. L. Gain, G. H. Paulino, Phase-field based topology optimization with

polygonal elements: a finite volume approach for the evolution equation, Struct. Multidisc. Optim. 46 (3) (2012) 327–342.

[49] A. Takezawa, M. Kitamura, Phase field method to optimize dielectric devices for electromagnetic wave propagation, J. Comput. Phys. 257PA (2014) 216–240.

[50] G. Allaire, Conception Optimale De Structures, Springer-Verlag, Berlin, 2007.

List of all figures

13. (a) Optimal configuration considering both stress and thermal constraints under a high heat flux and its (b) stress and (c) temperature distributions.
14. (a) Optimal configuration considering both stress and thermal constraints under a high temperature condition and its (b) stress and (c) temperature distributions.
15. Maximum von Mises stress for various heat fluxes of the optimal configuration of the (a) L-shape structure and (b) bridge-like structure. The dotted line indicates the allowable stress.
16. (a) Optimal configuration considering both stress and thermal constraints under multi thermal conditions and its stress distributions under (b) low heat flux and (c) high heat flux.
17. Maximum von Mises stress for various heat fluxes of the optimal configuration obtained under multi-thermal conditions. The dotted line indicates the allowable stress.

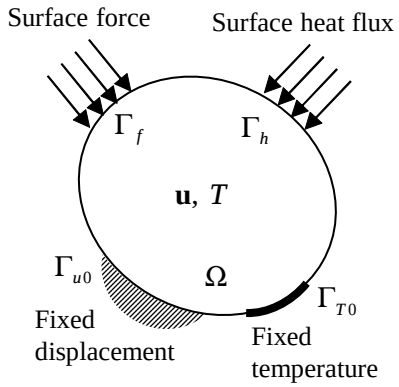

Figure 1: A linear elastic domain with surface force and heat flux.

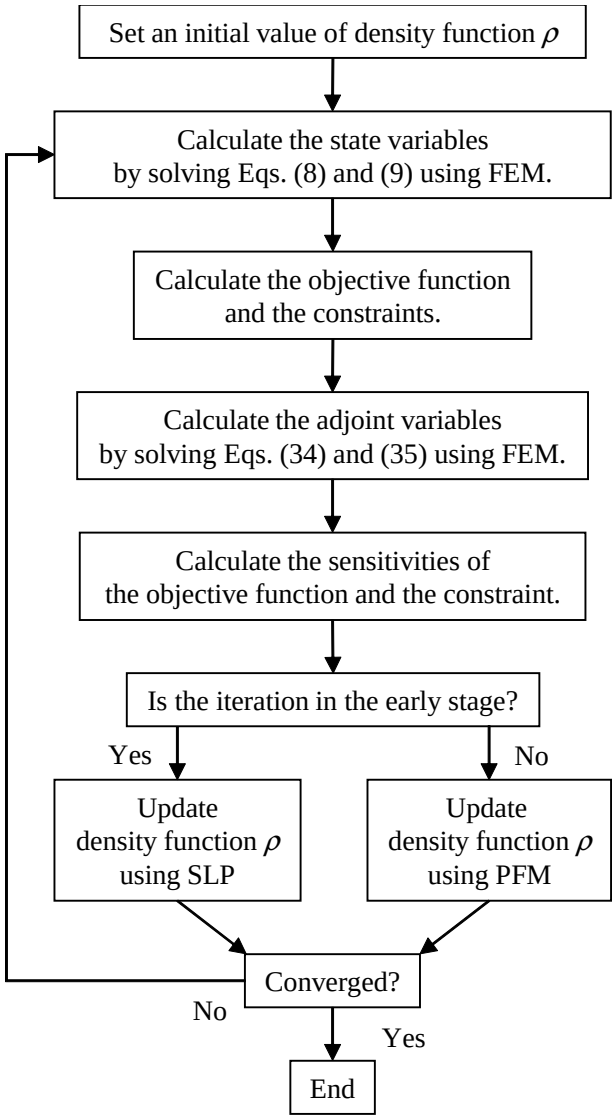

Figure 2: Flowchart of the optimization algorithm.

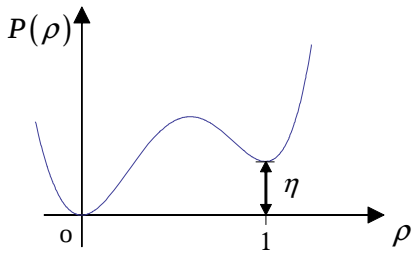

Figure 3: Outline of the double-well potential used in the PFM.

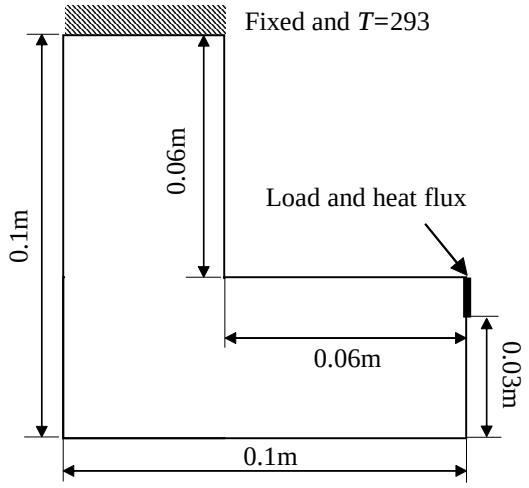

Figure 4: Design domain of the L-shaped structure.

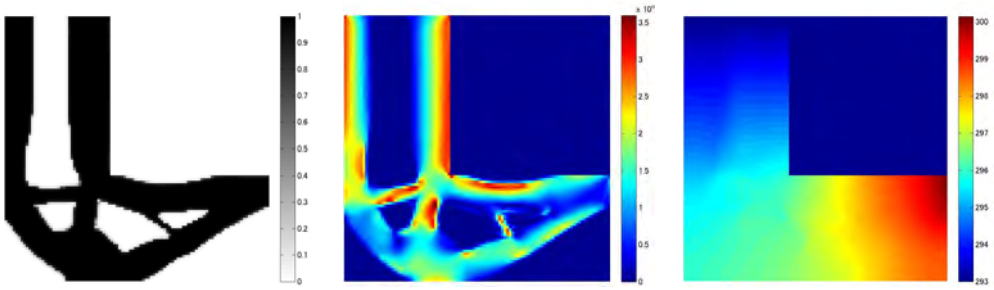

(a) (b) (c)

Figure 5: (a) Optimal configuration considering both stress and thermal constraints and its (b) von Mises stress and (c) temperature distributions.

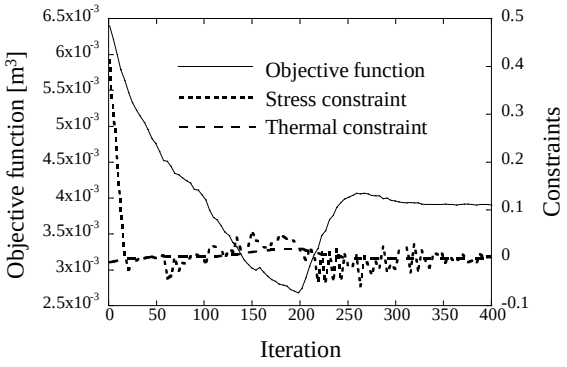

Figure 6: Convergence history of the objective function and constraints.

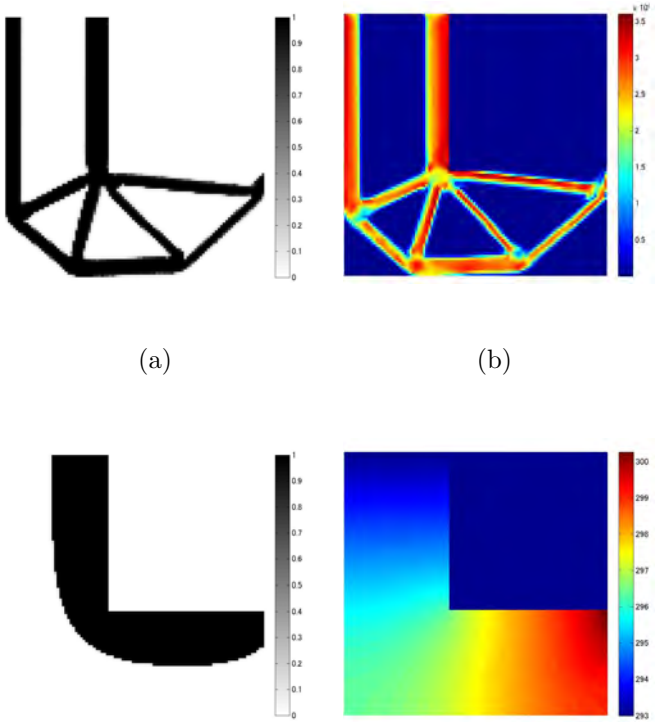

(a) (b)

(c) (d)

Figure 7: (a) Optimal configuration only considering the stress constraint and (b) its stress distribution. (c) Optimal configuration only considering the thermal constraint and (d) its temperature distribution.

(a) (b)

(c)

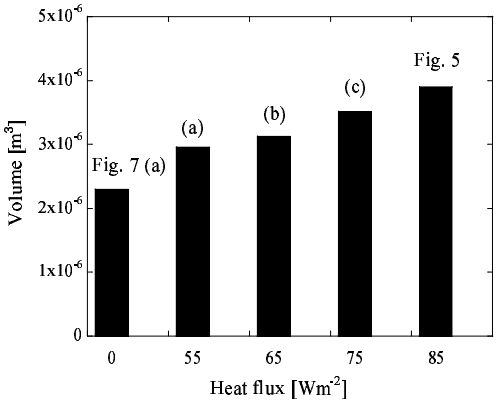

(d)

Figure 8: (a), (b) and (c) Optimal configuration considering both stress and thermal constraints obtained under various thermal conditions. (d) Comparison of volume in each figure.

(a) (b)

(c)

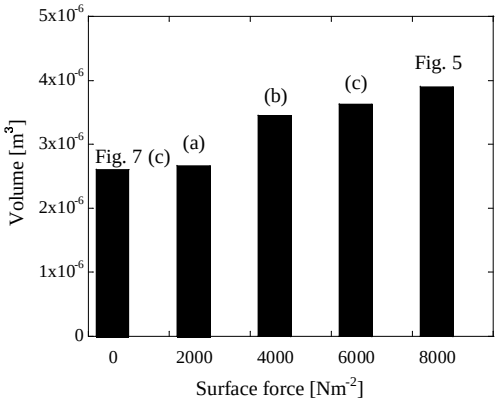

(d)

Figure 9: (a), (b) and (c) Optimal configuration considering both stress and thermal constraints obtained under various force conditions. (d) Comparison of volume in each figure.

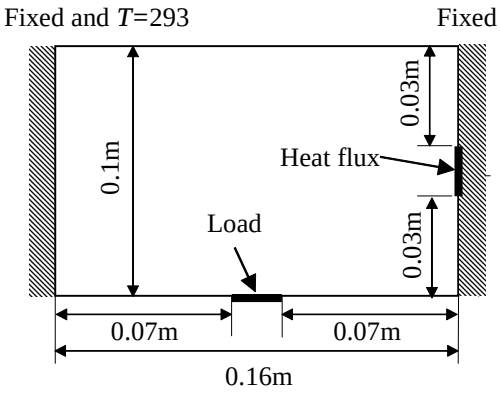

Figure 10: Design domain of the bridge-like structure.

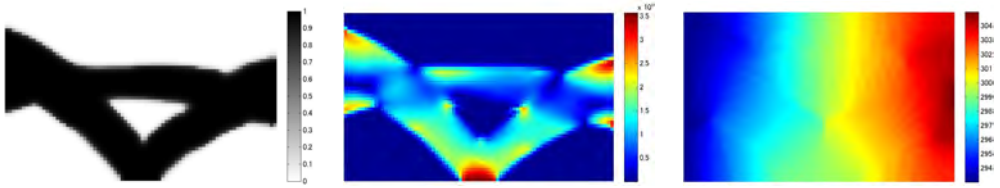

(a) (b) (c)

Figure 11: (a) Optimal configuration considering both stress and thermal constraints and its (b) stress and (c) temperature distributions for the bridge example.

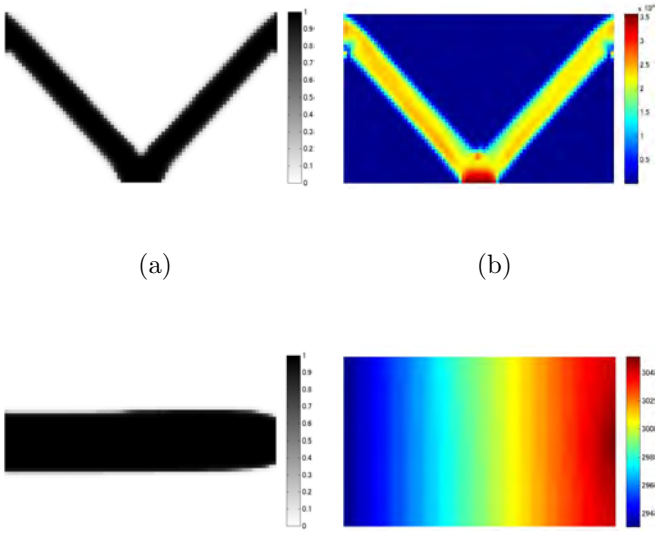

(a) (b)

(c) (d)

Figure 12: (a) Optimal configuration only considering the stress constraint and (b) its stress distribution. (c) Optimal configuration only considering the thermal constraint and (d) its temperature distribution.

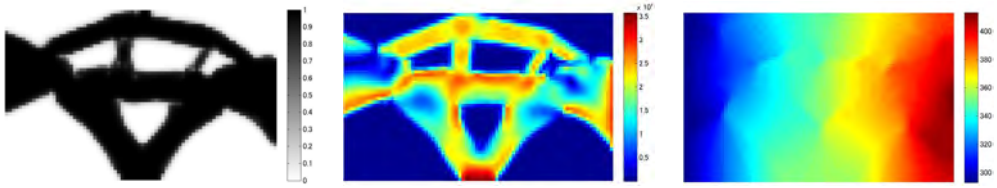

(a) (b) (c)

Figure 13: (a) Optimal configuration considering both stress and thermal constraints under a high heat flux and its (b) stress and (c) temperature distributions.

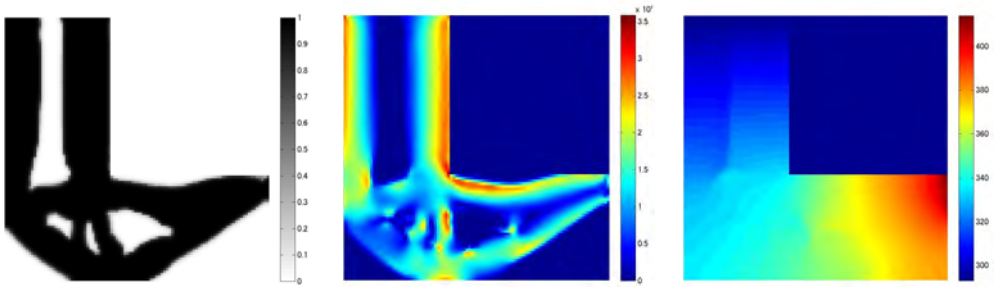

(a) (b) (c)

Figure 14: (a) Optimal configuration considering both stress and thermal constraints under a high temperature condition and its (b) stress and (c) temperature distributions.

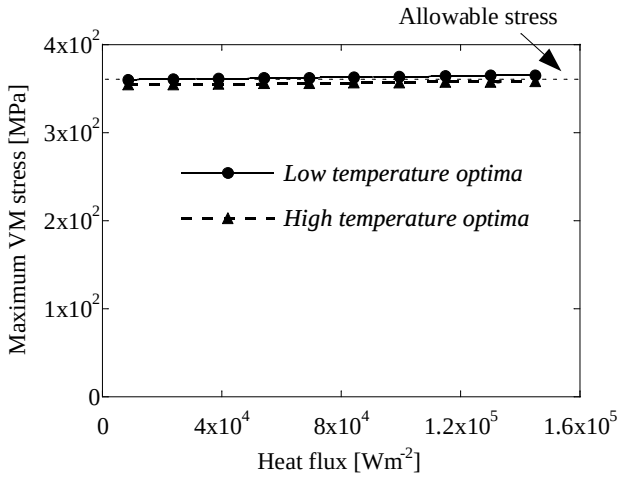

(a)

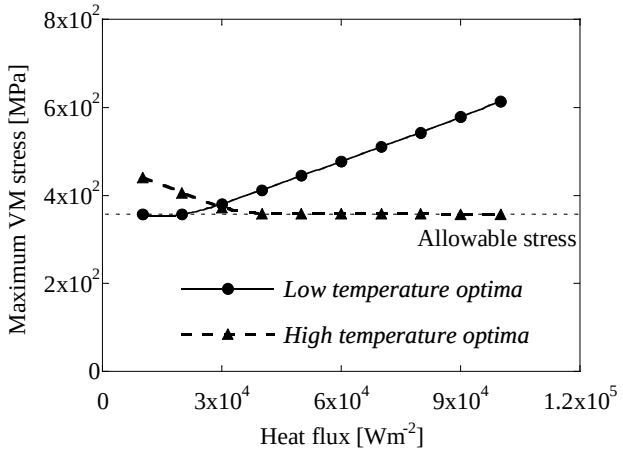

(b)

Figure 15: Maximum von Mises stress for various heat fluxes of the optimal configuration of the (a) L-shape structure and (b) bridge-like structure. The dotted line indicates the allowable stress.

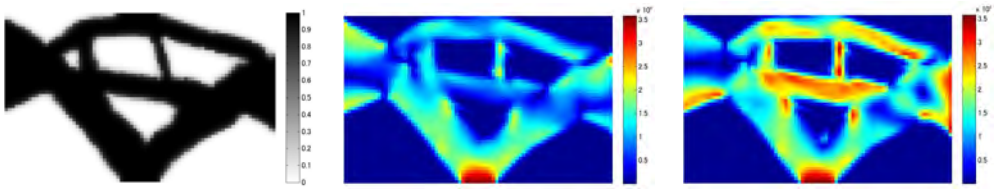

(a) (b) (c)

Figure 16: (a) Optimal configuration considering both stress and thermal constraints under multi thermal conditions and its stress distributions under (b) low heat flux and (c) high heat flux.

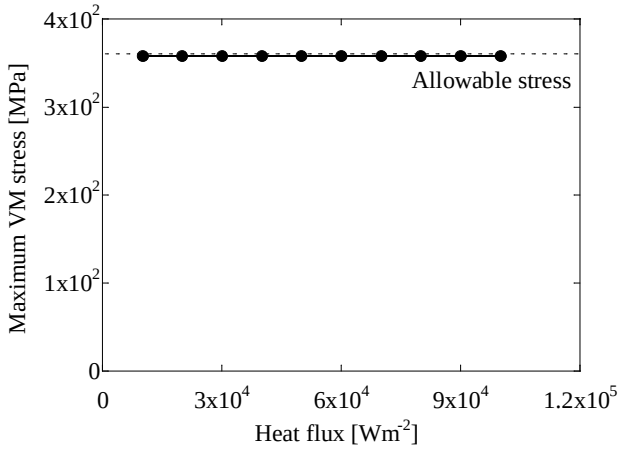

Figure 17: Maximum von Mises stress for various heat fluxes of the optimal configuration obtained under multi-thermal conditions. The dotted line indicates the allowable stress.